

# Harmonic Analysis of Modular Multilevel Matrix Converter for Fractional Frequency Transmission System

Jiajie Luo, Xiao-Ping Zhang <sup>1</sup>, Senior Member, IEEE, Ying Xue <sup>2</sup>, Member, IEEE, Kanghui Gu <sup>3</sup>, and Feng Wu <sup>4</sup>

**Abstract**—Fractional Frequency Transmission is a competitive technology for offshore wind power transmission. Modular Multilevel Matrix Converter (M<sup>3</sup>C) plays a key role in a Fractional Frequency Transmission System (FFTS) as the frequency changer. M<sup>3</sup>C is broadly considered as the AC–AC converter for the future with its attractive advantages in high voltage and high power applications. Due to the lack of a DC link, electrical quantities at different frequencies from two AC systems couple in M<sup>3</sup>C, resulting in a complex harmonic condition. Harmonics can lead to stability issues and its analysis is of great importance. This paper focuses on the harmonic analysis of M<sup>3</sup>C. The arm capacitor voltage ripples and the harmonic currents are analyzed at various frequencies. Major factors influencing the harmonics magnitude are discussed. Analysis is conducted on sub-module capacitance and arm inductance selection. A zero-sequence current mitigation controller for M<sup>3</sup>C is implemented and tested. It is found that for a FFTS, some current harmonics flow into AC systems even though the system is balanced, while the others circulate within the converter. The theoretical harmonic analysis is verified by simulations in Real Time Digital Simulator (RTDS) of a M<sup>3</sup>C system where each arm consists of forty sub-modules.

**Index Terms**—Fractional frequency transmission system, harmonic analysis, modular multilevel matrix converter (M<sup>3</sup>C), offshore wind power, energy storage.

## I. INTRODUCTION

UNDER the pressure of fossil energy depletion and environmental pollution, renewable energy development has drawn worldwide attention. Offshore wind power is favored with merits of not taking up land in cities, rich and stable resource and suitability for large-scale development. Three main offshore

wind transmission methods are traditional HVAC, HVDC and Fractional Frequency Transmission (FFT) [1]. FFT was first proposed in [2], the principle is to use a proportion of the system frequency, mostly 1/3, for the generator side. FFT requires less charging reactive current for cables than traditional HVAC, and therefore can support much longer transmission distance. Compared with HVDC, one main advantage is that no offshore converter station is needed. That means, not only for investment, but also for operation and maintenance, FFT is more economical within certain distance range, usually between 80 km and 180 km [3]. Most of the wind power plant projects that were built or planned lie in this range [4], [5] studied the feasibility of FFT and it showed a lower annual cost of FFT than HVDC. In addition, DC circuit breaker technology is still immature, and therefore the connection between the offshore wind farm and the onshore AC system is limited to point-to-point HVDC connections. Reliability suffers due to this reason and the situation would get worse when the level of offshore wind power penetration becomes high. On the contrary, FFT is not limited to point-to-point, and offshore grids are easy to form [6].

There is no doubt that frequency changer is the core component of FFT. Early-stage research has been focused on the use of cycloconverter [7], [8]. However, it was later proven that cycloconverter might not be suitable for offshore wind integration with defects of poor controllability, severe harmonics and unsatisfactory fault ride through ability [3]. Instead, M<sup>3</sup>C presents its strength in this application. Low voltage harmonic level, low switching loss, flexible scalability and controllable power factor make M<sup>3</sup>C outstanding as the next-generation AC-AC converter, particularly in high voltage applications like offshore wind power transmission [9].

M<sup>3</sup>C was introduced in 2001 in [10]. The topology is similar with the traditional matrix converter but there are significant differences with the inclusion of multilevel H-bridge sub-modules. Two main applications of M<sup>3</sup>C are motor driving [11]–[13] and wind energy transmission [9], [14], [15]. In [11], a control strategy for M<sup>3</sup>C based on dq transformation was proposed for motor driving and it was validated by experiment using a 400 V, 15 kW prototype. [12] optimized the inductors in M<sup>3</sup>C so that significant reductions in size and weight could be brought. The effectiveness was verified by a downscaled motor drive system. For wind energy transmission, different from that of motor drives, voltage rating is high and the sub-module number is large for M<sup>3</sup>C. Also the frequencies on both sides of M<sup>3</sup>C

Manuscript received November 13, 2018; revised March 28, 2019 and July 2, 2019; accepted August 16, 2019. Date of publication October 21, 2019; date of current version May 21, 2020. This work was supported in part by EPSRC Grants EP/N032888/1, EP/L017725/1, and EP/K006312/1 and in part by 111 Project “Renewable Energy Generation and smart grid” at Hohai University. This work was also sponsored by 111 Project “Renewable Energy Generation and smart grid” at Hohai University. Paper no. TPWRD-01403-2018. (Corresponding author: Xiao-Ping Zhang.)

J. Luo, X.-P. Zhang, and Y. Xue are with the Department of Electronic, Electrical and Systems Engineering, University of Birmingham, Birmingham B15 2TT, U.K. (e-mail: jxl394@student.bham.ac.uk; x.p.zhang@bham.ac.uk; y.xue@bham.ac.uk).

K. Gu and F. Wu are with the Department of Electronic, Electrical and Systems Engineering, University of Birmingham, Birmingham B15 2TT, U.K., and also with the College of Energy and Electrical Engineering, Hohai University, Nanjing 210098, China (e-mail: gukanghui@sina.com).

Color versions of one or more of the figures in this article are available online at <http://ieeexplore.ieee.org>.

Digital Object Identifier 10.1109/TPWRD.2019.2939312

are controlled to be constant. This paper focuses on this kind of application. In [15],  $M^3C$  was used in FFTS and its performance based on a new space vector modulation (SVM) control scheme was evaluated. As  $M^3C$  is further developed, it has been found that the number of space vectors grew exponentially with the increasing number of sub-modules. Consequently, SVM is unlikely to be implemented in wind power transmission application which requires a large number of sub-modules. A novel current control method of  $M^3C$  was developed in [16], featuring in the decoupling of input and output. In [9], this method was further improved for FFTS by introducing the cross synchronous rotating frames, so that DC values are dealt with at most time in current loops. In [14], a feedforward compensation strategy was proposed. Simulation results show that with the proposed control method,  $M^3C$  can cope with unbalanced grid conditions. Although plenty of work on  $M^3C$  control has been carried out, limited attention has been paid on the harmonic analysis of  $M^3C$ . Based on ideal assumptions, paper [17] derived the current expression of one arm of  $M^3C$ . The focus was on parameters selection of the capacitor and harmonic was not fully analyzed for all nine arms in  $M^3C$ . Authors of [18] provided an analysis of  $M^3C$  in FFTS. A mathematical model of a sub-converter was presented and verified, but no attention was paid to the harmonics.

For offshore wind power transmission system, harmonic analysis is vital from the stability point of view, as the generator side is a weak AC system and is prone to stability issues. It is shown that resonance and harmonic instability phenomena can occur when fast-switching devices interact with each other [19], [20]. Harmonic interaction was reported in [21] in the BorWin1 offshore wind farm system. The incident resulted in an outage of the HVDC system and wind power was not able to be transmitted. Harmonic analysis is also crucial to prevent device damage and economic loss. [22] reveals that for MMC, with the sub-module capacitor voltage ripple and harmonic currents, even the harmonic currents only circulate within the converter and do not flow into the grid, there exist poorly damped resonant modes that can lead to harmonic instability. In a MMC-HVDC system, [23] shows that circulating currents are in even orders, mainly in second order and they are confined within the converter. Besides, both the second order capacitor voltage and arm voltage are in negative sequence. However, the harmonic situation for a  $M^3C$  based FFTS is still not clear, which is the main focus of this paper. Undoubtedly, MMC and  $M^3C$  have similarities and they are often compared as counterparts. Nevertheless, without a DC link in  $M^3C$ , two frequencies intertwine in the converter, and hence the harmonic situation is fundamentally different from that in MMC.

The contributions of the paper are summarized as follows.

- A harmonic analysis method for  $M^3C$  is proposed. This method analyzes how the harmonic components are generated and it is compatible with different applications.
- Current harmonics at multiple frequencies are quantified. Based on the analysis, they are classified into three types. It is indicated that some current harmonics circulate in arms, some behave as positive-sequence fundamental current and the others are zero-sequence and flow into AC systems.

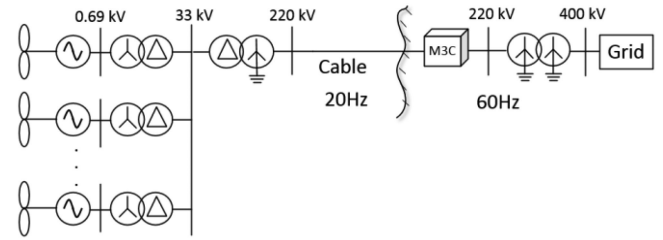


Fig. 1. The configuration of an offshore wind FFTS.

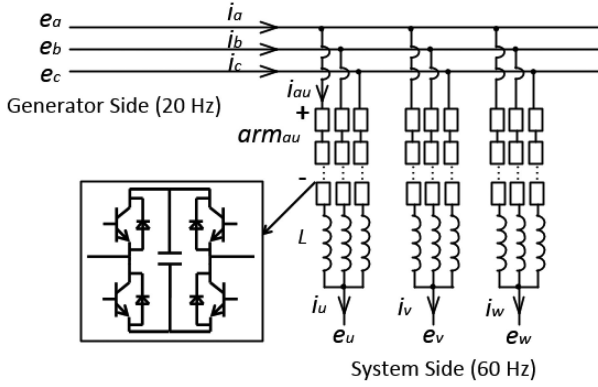
- Factors that have large impacts on harmonic magnitude are studied. Also, the influences of the harmonic components on  $M^3C$  itself and AC systems are discussed in a detailed manner. The analysis provides insights to  $M^3C$  modelling and can serve for the development of new control method.
- Guidelines are provided on sub-module capacitance and arm inductance selection to limit capacitor voltage ripple and harmonic current distortion. An effective zero-sequence current mitigation controller for  $M^3C$  is designed.

The rest of the paper is organized as follows. Section II introduces the  $M^3C$  for offshore wind FFTS. The current and voltage relations for one sub-module are derived first, and then the whole arm consisting all sub-modules is considered. Section III conducts a harmonic analysis of the  $M^3C$  for FFTS. Different components are quantified and classified. The influences of different harmonic components are discussed. In Section IV, time-domain simulation results are presented to confirm the correctness of the analysis. Finally, conclusions are provided in Section V.

## II. $M^3C$ FOR OFFSHORE WIND FFTS

Similar to traditional HVAC transmission, a schematic diagram of an offshore wind FFTS is displayed in Fig. 1. The grid side frequency is chosen to be 60 Hz and the offshore wind farm generates power at 1/3 of the system frequency, which is 20 Hz. The voltage is stepped up by the transformers and then the wind power is transmitted onshore at fractional frequency. The  $M^3C$  station which locates onshore triples the frequency and delivers the power into the main grid. The configuration of the  $M^3C$  is shown in Fig. 2.  $e_a, e_b, e_c$  and  $i_a, i_b, i_c$  on the left refer to three-phase voltages and currents at the offshore wind generator side. Similarly, quantities with  $u, v, w$  are system side voltages and currents. Each phase of the fractional frequency side is connected to all three phases of the system side respectively. The positive direction of current is from generator to system. The positive polarities of voltages are as shown in Fig. 2. There are nine arms in total and each arm consists of a number of IGBT-based full bridge sub-modules. In one arm, the switching signal of the  $i^{\text{th}}$  sub-module  $S_{\text{armi}}$  can be defined as:

$$\begin{cases} S_{\text{armi}} = 1, & (u_{dc} \text{ inserted}) \\ S_{\text{armi}} = 0, & (\text{bypassed}) \\ S_{\text{armi}} = -1, & (-u_{dc} \text{ inserted}) \end{cases} \quad (1)$$


 Fig. 2. Schematic diagram of a M<sup>3</sup>C.

Assuming that the sub-module voltages are balanced at steady state, the capacitor voltage  $u_{dc}$  for every sub-module in an arm is the same. The current relation for one sub-module can be expressed as:

$$S_{\text{armi}} i_{\text{arm}} = C \frac{du_{dc}}{dt} \quad (2)$$

where  $i_{\text{arm}}$  is the arm current,  $C$  is the capacitance of one sub-module. Refer  $N$  to the total sub-module number in an arm. Summing up (2) for all sub-modules in the arm, the current relation becomes:

$$\sum_{i=1}^N S_{\text{armi}} i_{\text{arm}} = NC \frac{du_{dc}}{dt} \quad (3)$$

$$n i_{\text{arm}} = NC \frac{du_{dc}}{dt}$$

where  $n$  is the difference between the number of  $u_{dc}$  inserted sub-modules and that of  $-u_{dc}$  inserted ones. Considering that sub-modules are inserted in only one direction at normal operation,  $n$  can be referred to the number of the inserted sub-modules (negative value means sub-modules are inserted with  $-u_{dc}$ ). Define  $S_{\text{arm}}$  as the average switching function of an arm, which is the ratio between inserted sub-module number and total sub-module number ( $n/N$ ). This yields the current relation of a M<sup>3</sup>C arm:

$$S_{\text{arm}} i_{\text{arm}} = C \frac{du_{dc}}{dt} \quad (4)$$

The voltage relation of a M<sup>3</sup>C arm can be written as (5), where  $u_{\text{arm}}$  is the arm voltage.

$$u_{\text{arm}} = NS_{\text{arm}} u_{dc} \quad (5)$$

Equation (4) and (5) describe both the voltage and current relations for a M<sup>3</sup>C arm. The same equations are applied to all nine arms of M<sup>3</sup>C.

### III. HARMONIC ANALYSIS OF M<sup>3</sup>C FOR OFFSHORE WIND FFTS

Frequencies from the generator side  $\omega_1$  and the system side  $\omega_3$  couple in M<sup>3</sup>C. At balanced steady state, the phase current

is equally spread in three arms [17], [18]. For example, the arm current  $i_{au}$  contains one third of the phase current  $i_a$ , one third of the phase current  $i_u$ , and also harmonics. The arm currents can be expressed as:

$$i_{\text{arm}} = \frac{1}{3}i_{20} + \frac{1}{3}i_{60} + i_{\text{arm}}^{\text{harmonics}} \quad (6)$$

where  $i_{20}$  and  $i_{60}$  are the phase currents from the generator side and the grid side respectively.  $i_{\text{arm}}^{\text{harmonics}}$  is the arm harmonics which will be discussed later in this section. When the harmonic current is insignificant, arm currents for all nine arms can be given as:

$$i_{au} \approx \frac{1}{3}I_a \sin(\omega_1 t + \beta_1) + \frac{1}{3}I_u \sin(\omega_3 t + \beta_3)$$

$$i_{av} \approx \frac{1}{3}I_a \sin(\omega_1 t + \beta_1) + \frac{1}{3}I_u \sin(\omega_3 t + \beta_3 - 120) .$$

$$i_{cw} \approx \frac{1}{3}I_a \sin(\omega_1 t + \beta_1 + 120) + \frac{1}{3}I_u \sin(\omega_3 t + \beta_3 + 120) \quad (7)$$

where  $I_a$ ,  $I_u$ ,  $\beta_1$  and  $\beta_3$  are the magnitudes and phase angles of the generator side and system side current respectively. Also, the arm switching functions can be given by:

$$S_{au} = m_a \sin(\omega_1 t + \alpha_1) - m_u \sin(\omega_3 t + \alpha_3)$$

$$S_{av} = m_a \sin(\omega_1 t + \alpha_1) - m_u \sin(\omega_3 t + \alpha_3 - 120)$$

$$S_{cw} = m_a \sin(\omega_1 t + \alpha_1 + 120) - m_u \sin(\omega_3 t + \alpha_3 + 120) \quad (8)$$

where  $m_a$ ,  $m_u$ ,  $\alpha_1$  and  $\alpha_3$  are the generator side and system side voltage modulation ratios and angles.

#### A. Capacitor Voltage Ripples

Apply (4) to arm  $au$ , the capacitor voltage can be expressed as:

$$u_{dc\_au} = \int \frac{1}{C} S_{au} i_{au} \quad (9)$$

Substitute  $i_{au}$  in (7) and  $S_{au}$  in (8) into (9), the expression of the capacitor voltage in arm  $au$  can be derived. The expressions of the rest eight arms can be acquired in the same manner. The arm current and the switching function both contain harmonic components at frequencies  $\omega_1$  and  $\omega_3$ . According to trigonometric product-to-sum identity, the capacitor voltage frequency spectrum contains  $2\omega_1$ ,  $2\omega_3$ ,  $(\omega_3 \pm \omega_1)$  and 0 Hz components. In this section and later analysis, the system frequency is considered to be 60 Hz. In this case, beside the DC component, the capacitor voltage has ripples of 40 Hz (also 80 Hz and 120 Hz). These frequencies are different from frequencies at either side of the ac systems. The 40 Hz voltage ripple has the largest magnitude compared to components at other frequencies. This will be further discussed and verified by the time domain

TABLE I  
ARM FREQUENCY COMPONENTS

Frequency (Hz)	Components (/Hz)
20	(20 + DC); (40 - 20); (60 - 40)
60	(60 + DC); (20 + 40)
100	(60 + 40)

simulation in Section IV. The constituent terms at 40 Hz are analyzed and the full expressions are calculated and shown as:

$$\begin{aligned}
u_{dc_{au40}} &= k_1[-m_a I_a \sin(\theta_1) + m_a I_u \sin(\theta_2) \\
&\quad - m_u I_a \sin(\theta_3)] \\
u_{dc_{av40}} &= k_1[-m_a I_a \sin(\theta_1) + m_a I_u \sin(\theta_2 - 120) \\
&\quad - m_u I_a \sin(\theta_3 - 120)] \\
u_{dc_{aw40}} &= k_1[-m_a I_a \sin(\theta_1) + m_a I_u \sin(\theta_2 + 120) \\
&\quad - m_u I_a \sin(\theta_3 + 120)] \\
&\quad \vdots \\
u_{dc_{bu40}} &= k_1[-m_a I_a \sin(\theta_1 + 120) + m_a I_u \sin(\theta_2 - 120) \\
&\quad - m_u I_a \sin(\theta_3 - 120)] \\
&\quad \vdots \\
u_{dc_{bv40}} &= k_1[-m_a I_a \sin(\theta_1 - 120) + m_a I_u \sin(\theta_2) \\
&\quad - m_u I_a \sin(\theta_3)]
\end{aligned} \tag{10}$$

where:  $k_1 = \frac{1}{12C\omega_1}$ ;  $\theta_1 = 2\omega_1 t + \alpha_1 + \beta_1$ ;  $\theta_2 = 2\omega_1 t + \beta_3 - \alpha_1$ ;  $\theta_3 = 2\omega_1 t + \alpha_3 - \beta_1$

As can be seen from (10), the 40 Hz component of the capacitor voltage consists of three terms. For each term, the magnitude is the same for all nine arms while there can be a phase shift between nine arms. When the high order components are neglected, the capacitor voltage can be expressed as the sum of the dc component and the 40 Hz component:

$$u_{dc} \approx u_{dc_0} + u_{dc_40} \tag{11}$$

### B. Arm Current Harmonics

The purpose of this part is to analyze the arm currents of the M<sup>3</sup>C at various frequencies. In order to derive the expression of the arm currents, arm voltages are derived first. Then together with KVL equations, the arm currents are acquired so that the harmonics can be analyzed.

In (8), switching function is of 20 Hz and 60 Hz. And in (11), capacitor voltage is of DC and 40 Hz. Substitute (8) and (11) into (5), components at different frequencies appear in arm voltage, which are shown in Table I. As can be seen, arm voltage contains components at 20 Hz, 60 Hz and 100 Hz. How each component is generated is shown in the second column in Table I. For instance, switching function at 60 Hz and capacitor voltage at 40 Hz gives arm voltage at 100 Hz and 20 Hz. The terms (20 + DC) and (60 + DC) are in positive sequence and they relate to the positive-sequence fundamental currents. These two

terms do not belong to the scope of harmonics and will not be analyzed.

According to KVL, equations at 20 Hz, 60 Hz and 100 Hz can be written as:

$$\begin{aligned}
e_a &= u_{arm\_au\_20} + L \frac{di_{au\_20}}{dt} \\
0 &= u_{arm\_au\_60} + L \frac{di_{au\_60}}{dt} + e_u \\
0 &= u_{arm\_au\_100} + L \frac{di_{au\_100}}{dt}
\end{aligned} \tag{12}$$

As KVL does not alter frequency, the frequency components of the arm current remain the same as the ones of the arm voltage as Table I shows. Combine (5), (8) and (10–12), current harmonics at 20 Hz, 60 Hz and 100 Hz can be calculated.

1) *100 Hz*: The expression of the arm currents at 100 Hz is shown in (13).  $\omega_5$  is referred to the frequency at 100 Hz. The arm currents at 100 Hz are formed of three terms. For each term, the magnitude is the same for all nine arms. Adding up  $i_{au100}$ ,  $i_{av100}$  and  $i_{aw100}$ , all three terms cancel out, which means that the arm currents at 100 Hz will not flow into phase a and exist only in the arm. Same rule applies to phase b and c, and therefore the arm currents at 100 Hz are isolated from the generator side AC system. In terms of the system side, the same procedure is carried out. Likewise,  $i_{aw100}$ ,  $i_{bw100}$  and  $i_{cw100}$  add up to zero (same for phase u and v) so no current at 100 Hz will flow into the system side. In conclusion, the natures of these currents are circulating currents which only circulate within the converter. They take up the current rating of the semiconductor devices and should be suppressed during operation.

$$\begin{aligned}
i_{au100} &= k_2[m_u m_a I_a \sin(\theta_4) - m_u m_a I_u \sin(\theta_5) \\
&\quad + m_u^2 I_a \sin(\theta_6)] \\
i_{av100} &= k_2[m_u m_a I_a \sin(\theta_4 - 120) - m_u m_a I_u \sin(\theta_5 + 120) \\
&\quad + m_u^2 I_a \sin(\theta_6 + 120)] \\
i_{aw100} &= k_2[m_u m_a I_a \sin(\theta_4 + 120) - m_u m_a I_u \sin(\theta_5 - 120) \\
&\quad + m_u^2 I_a \sin(\theta_6 - 120)] \\
&\quad \vdots \\
i_{bw100} &= k_2[m_u m_a I_a \sin(\theta_4 - 120) - m_u m_a I_u \sin(\theta_5) \\
&\quad + m_u^2 I_a \sin(\theta_6)] \\
&\quad \vdots \\
i_{cw100} &= k_2[m_u m_a I_a \sin(\theta_4) - m_u m_a I_u \sin(\theta_5 + 120) \\
&\quad + m_u^2 I_a \sin(\theta_6 + 120)]
\end{aligned} \tag{13}$$

where:  $k_2 = \frac{N}{24LC\omega_1\omega_5}$ ;  $\theta_4 = \omega_5 t + \alpha_3 + \alpha_1 + \beta_1$ ;  $\theta_5 = \omega_5 t + \alpha_3 + \beta_3 - \alpha_1$ ;  $\theta_6 = \omega_5 t + 2\alpha_3 - \beta_1$

2) *60 Hz*: According to Table I, there are two sources of the 60 Hz arm currents. The first one is fundamental current and does not need to be analyzed. The expression of the second component is calculated and shown in (14). As it shows, the first of the three terms of the arm currents at 60 Hz has the same magnitude and phase angle for all nine arms of M<sup>3</sup>C. As a result, it behaves as zero-sequence current for AC systems at both sides and it flows

TABLE II  
20 Hz ARM CURRENT

Frequency (Hz)		Generator Side	System Side
(40 - 20)	Term1	Positive sequence	Cancelled out
	Term2&3	Cancelled out	Cancelled out
(60 - 40)	Term1	Cancelled out	Cancelled out
	Term2&3	Positive sequence	Cancelled out

into both systems with equal magnitude if no countermeasure was implemented. This current is undesirable since it causes current distortion and can bring further instability issues like harmonic interaction and resonance. For the rest two terms, they cancel out at the fractional frequency side and are of positive sequence at the system side. They behave like the fundamental current and can be regulated by the current controller in vector control. The positive-sequence components are not problematic and strictly speaking, they do not belong to the harmonic scope.

$$\begin{aligned}
i_{au60\_2} &= k_3[-m_a^2 I_a \sin(\theta_7) + m_a^2 I_u \sin(\theta_8) \\
&\quad - m_a m_u I_a \sin(\theta_9)] \\
i_{av60\_2} &= k_3[-m_a^2 I_a \sin(\theta_7) + m_a^2 I_u \sin(\theta_8 - 120) \\
&\quad - m_a m_u I_a \sin(\theta_9 - 120)] \\
i_{aw60\_2} &= k_3[-m_a^2 I_a \sin(\theta_7) + m_a^2 I_u \sin(\theta_8 + 120) \\
&\quad - m_a m_u I_a \sin(\theta_9 + 120)] \\
&\quad \vdots \\
i_{bu60\_2} &= k_3[-m_a^2 I_a \sin(\theta_7) + m_a^2 I_u \sin(\theta_8 + 120) \\
&\quad - m_a m_u I_a \sin(\theta_9 + 120)] \\
&\quad \vdots \\
i_{cw60\_2} &= k_3[-m_a^2 I_a \sin(\theta_7) + m_a^2 I_u \sin(\theta_8 + 120) \\
&\quad - m_a m_u I_a \sin(\theta_9 + 120)]
\end{aligned} \tag{14}$$

where:  $k_3 = \frac{N}{24LC\omega_1\omega_3}$ ;  $\theta_7 = \omega_3 t + 2\alpha_1 + \beta_1$ ;  $\theta_8 = \omega_3 t + \beta_3$ ;  $\theta_9 = \omega_3 t + \alpha_1 + \alpha_3 - \beta_1$

3) 20 Hz: The harmonic currents at 20 Hz are analyzed by carrying out the same calculations to the second and the third terms of 20 Hz in Table I. Results are concluded in Table II. Detailed equations are available in the appendix. The first term of the component (40–20) Hz and the second and third terms of the component (60–40) Hz behave like the positive-sequence fundamental current. The second and third terms of the component (40–20) Hz and the first term of the component (60–40) Hz only exist in the arms and will not flow into AC systems.

To sum up, the components of the arm currents analyzed above can be classified into three types. The first type only circulates within the converter but does not flow into AC systems. The second type does not cancel out at terminals and therefore goes into AC systems as zero-sequence current. The third type acts like positive-sequence fundamental current. The affecting factors of

harmonic magnitude and influences of these harmonics on M<sup>3</sup>C itself and also AC systems connected to it are discussed in the following section.

### C. Affecting Factors and Influences of M<sup>3</sup>C Harmonic Components

As (13), (14), (A1) and (A2) show, the magnitude of these harmonic components depends on the sub-module capacitance, the inductance, the frequency of the AC system etc. The smaller the capacitance or the inductance, the larger the harmonics magnitude would be. If the AC system frequency is very small, in theory the harmonic components become infinity and the system could not function normally. Thus, the working frequency of the FFTS cannot be too low. In addition, current harmonics are related to capacitor voltage ripples. Effective ripple control is beneficial to harmonic suppression. Some of the current components coincide with the system frequency and are easy to omit.

Based on the analysis in Section B, it is indicated that there will be zero-sequence current flowing into the AC systems at both sides if no countermeasure was conducted. This can be problematic as wind farm is prone to stability problems [24]. Attention should also be paid to the system side, because offshore wind farms are often located in remote areas, where the strength of the AC network is weak [25]. Among three types of currents discussed in the last session, the components in positive sequence are not harmful since they can be regulated by the close-loop current controller. Circulating current and zero-sequence current can adversely influence the converter and AC systems in the following aspects:

- Both circulating and zero-sequence currents take up current rating of the power electronic devices. They raise thermal issues and degrade the semiconductors. For multilevel converters, high voltage can be achieved by stacking up sub-modules but current ability limits the power rating. In terms of an offshore wind power transmission project, converter capital cost is therefore increased.
- The zero-sequence currents can flow into the AC network, which bring additional losses in devices including transformers and AC motors and raise the operating temperature. The aging of devices is accelerated and power loss also leads to low efficiency.
- The harmonic currents flowing in the AC system can further cause instability problems. Large magnitude of zero-sequence current may trip the zero-sequence protection. When wind energy has high penetration, unexpected disconnection of a large wind power source would have significant effect on power system stability. Besides, harmonic interaction or resonance may happen. Torsional oscillation can be triggered in generators with the existence of injected harmonic currents. It results in shaft fatigue or even shaft failure [26], [27].

The transformer connection in an offshore wind power system based on real projects is shown in Fig. 1, with more details available in [28], [29]. The step-up transformer at the wind generator side usually includes delta connection, as a result of which, the zero-sequence currents could not reach the wind generator.

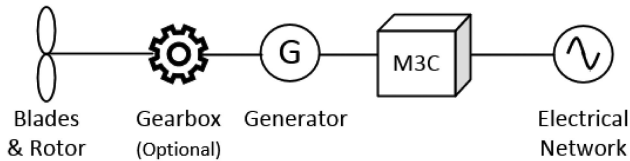


Fig. 3. Topology to connect a high power wind turbine via  $M^3C$ .

TABLE III  
SIMULATION PARAMETERS

Symbol	Quantity	Value
$S$	rated power	30 MVA
$f_1$	fractional frequency	20 Hz
$f_3$	system frequency	60 Hz
$V_{20}$	rated fractional frequency side voltage	33 kV
$V_{60}$	rated system side voltage	33 kV
$N$	sub-module number each arm	40
$u_{dc,ref}$	capacitor voltage reference	1.5 kV
$L$	inductance	15 mH
$C$	Sub-module capacitance	10 mF / 5 mF

However, for the system side, due to protection considerations at high voltage level (several hundred kV), transformers are normally in Wye/Wye connection with grounding. Wye/Wye transformer enjoys the advantages of fewer turns for winding, lower insulation level, no phase displacement and therefore is cheaper and suitable for high voltage applications. [30] Further action should be taken when the harmonic magnitude is large. Besides FFT, another topology (as shown in Fig. 3) that connects medium voltage high power wind turbine with  $M^3C$  is prosed in [13], [31]. In this application, maximum power point tracking can be achieved and good dynamic performance was validated. However, in terms of harmonics, zero-sequence currents can impede the wind generator and also the electrical network, so further measures should be taken. Undoubtedly, sub-module capacitance and arm inductance should be carefully selected to limit the harmonics. Besides, one option could be adopting delta winding for the grid-connecting transformer to cut off the path of the zero-sequence currents. However, in that case the benefits of the Wye/Wye transformer would no longer exist. Another solution is to leave the transformer unchanged, but adopt a closed-loop controller to suppress the zero-sequence currents using the controllability of  $M^3C$ . The control algorithm will be discussed and the effectiveness will be verified in Section V.

#### IV. SIMULATION RESULTS AND ANALYSIS VALIDATION

To validate the theoretical analysis, a  $M^3C$  connecting two AC systems at 20 Hz and 60 Hz is simulated in RTDS (See Fig. 2). Each arm has forty sub-modules. System at 20 Hz transmits power to 60 Hz side. Simulation parameters are provided in Table III. The  $M^3C$  simulated in RTDS is a detailed model and the simulation time step is set to  $3 \mu s$  to guarantee the accuracy of the simulation results where the MMC valves are modeled in the small time step.

In the ‘small time step’ modelling framework of RTDS, there are two different modelling methods developed, referred to as *Method A* and *Method B*, thereafter.

- *Method A*: In this method, modeling switching devices with the use of L and C was discussed in [33]. This method could lead to certain discrepancy if parameters were not set properly. Results between PSCAD and RTDS (small time step) were presented and compared in [33], which matched very well.
- *Method B*: In Method B, the MMC valve model in RTDS simulation also employs a resistive switching. Details of MMC valve model in RTDS using a resistive switching (Method B) can be found in [32]. In our simulations, ‘small time step’ Method B is used to model the MMC switching devices.

Method B models the MMC switching devices with the resistive switching approach, which is similar to that used in PSCAD. It may be useful to point out that due to calculation constraint, an artificial short interface line around 400 meters is inserted between the MMC arm component and the rest of the small time step circuit in RTDS. But since the application in this paper is offshore wind power transmission, whose distance is normally from tens of km to several hundred km, the impact of such a very short interface line on the accuracy of the overall system simulations is negligible. [32] conducted a thorough comparison on CIGRE DC grid test systems between RTDS MMC model using Method B and PSCAD MMC model to validate the correctness of the RTDS MMC valve model. All the cases showed very close results. In terms of actual values of the interface line parameters, C is in the magnitude of nF and this is so tiny that it can be ignored, and L is in the magnitude of mH, which can be taken out of the real arm inductance so that the total inductance remains the same. In addition, there are wires between arms in physical circuit, which justifies the rationality of the interface.

The assumptions can be verified and the theoretical analysis can be compared to simulation results. The control method adopted is the vector control with inner current loops and outer loops for active/reactive power control or capacitor voltage balancing control. More details of the control system can be found in [34]. Note that the capacitor voltage for the control input should be the filtered version to avoid influence of the controller on quantified analysis. Otherwise the controller would try to control the capacitor voltage ripple as well and would not match the theoretical calculation. A low pass filter is applied to the active power signal for the same consideration.

Line voltages and line currents at both generator side (20 Hz) and system side (60 Hz) are plotted in Fig. 4. It can be seen that line voltages are perfect sinusoidal waveforms while line currents have small amount of harmonics. Fig. 5 shows the arm voltages and arm currents of the  $M^3C$ . Both are mainly composed of 20 Hz and 60 Hz quantities, which can be reflected by (7) and (8). Furthermore, the 20 Hz arm voltage components of  $u_u$ ,  $u_v$  and  $u_w$  are extracted and plotted in Fig. 6a (left). As can be seen, three curves are overlapped, indicating that the arm voltages are balanced at the 20 Hz side. Similarly, the 60 Hz arm voltage components of  $u_u$ ,  $u_b$  and  $u_c$  are plotted in Fig. 6a

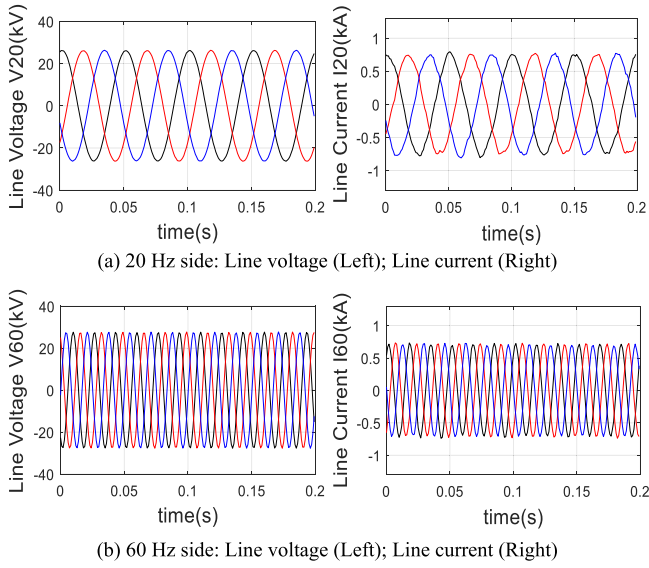


Fig. 4. Line voltage and line current at 20 Hz and 60 Hz sides.

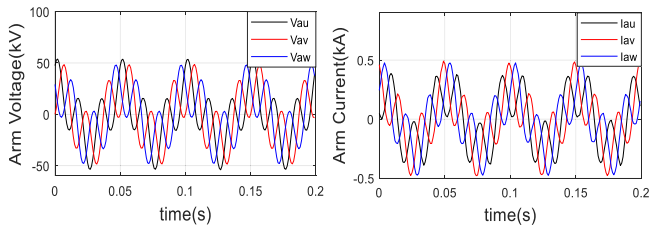


Fig. 5. Arm voltage (Left) and arm current (Right) of  $M^3C$ .

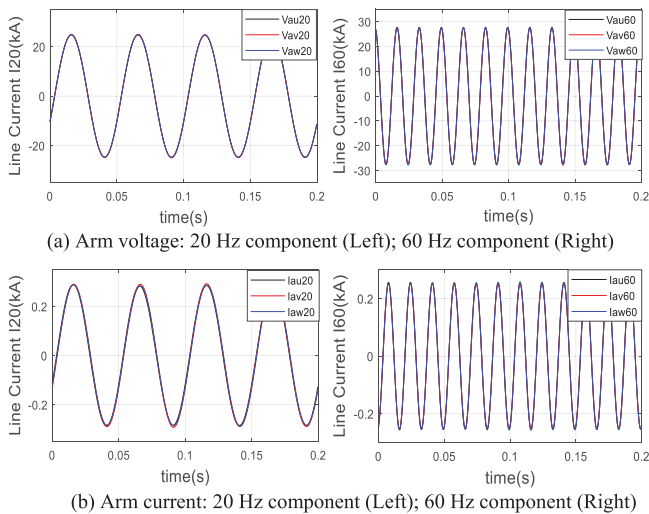


Fig. 6. 20 Hz and 60 Hz components of arm voltage and current.

(right) and the arm voltages are also balanced at the 60 Hz side. For the arm currents, same process is conducted and the current waveforms are of very minor difference, indicating that the AC side phase current spreads equally into the three arms connected to it. These results show that the assumptions described in

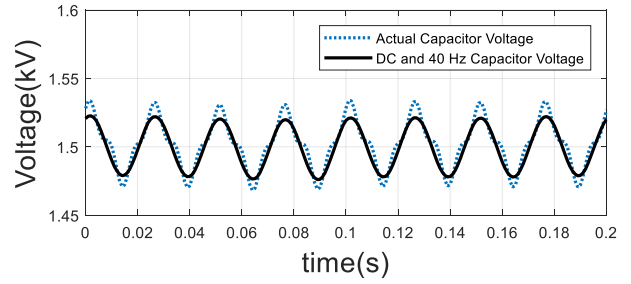


Fig. 7. Sub-module actual capacitor voltage and capacitor voltage with only dc and 40 Hz components.

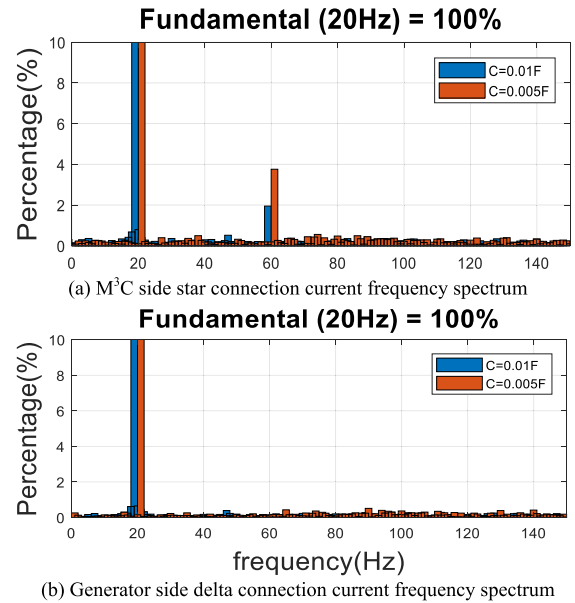


Fig. 8. Frequency spectrum of currents at 20 Hz Side.

Section I are valid at steady state and the performance of the  $M^3C$  as a frequency changer is satisfactory.

For capacitor voltage, the measured actual capacitor voltage (dotted line) is plotted together with the capacitor voltage being composed of only DC and 40 Hz component (solid line) in Fig. 7. As can be seen, the main capacitor voltage ripple is at 40 Hz, and the magnitude of components at 80 Hz, 120 Hz etc. is small. Therefore, neglecting higher frequency components only gives little discrepancy on capacitor voltage. When higher accuracy is required, the same analysis procedure can be repeated to include higher frequency ripples.

Then the harmonics at 20 Hz side is studied. YN/d connection is selected for the step-up transformer connecting the  $M^3C$  and the generator side, which can be shown in Fig. 1. The frequency spectrums of both sides of the transformer are plotted in Fig. 8. It can be seen in Fig. 8(a) that the 60 Hz harmonic current does flow into the 20 Hz side AC system. But due to the delta connection of the transformer, it is isolated from the generator side (See Fig. 8(b)) and has no effect on wind generators. Besides, two sets of capacitance values are chosen as 1 mF and 5 mF respectively. It can be observed that when the capacitance is halved,

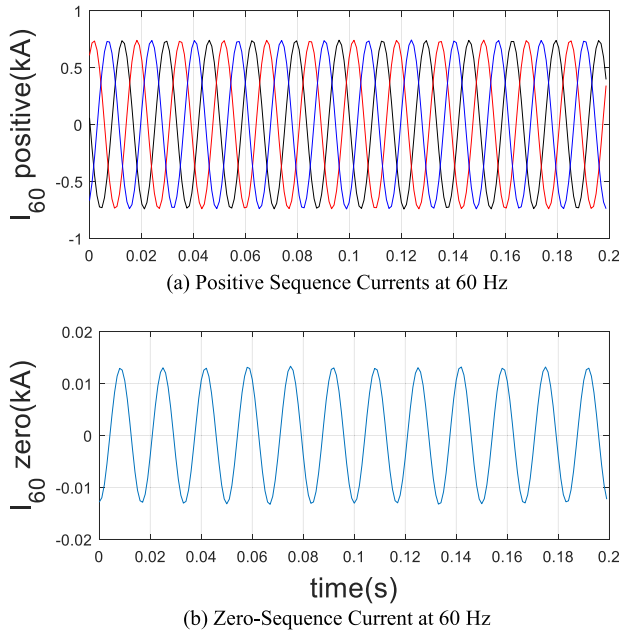


Fig. 9. Currents at 60 Hz Side.

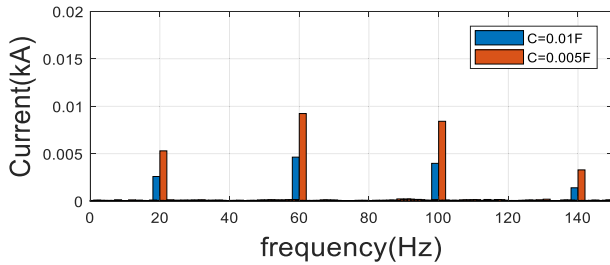


Fig. 10. Frequency spectrum of arm current harmonics.

the harmonic current magnitude doubles. Results validate the analysis in Section III.

On the system side, the line currents are measured and decomposed into positive-sequence currents and zero-sequence current. Fig. 9 shows that the positive-sequence currents peak at 0.68 kA while the zero-sequence current peaks at 0.013 kA. The magnitude of the zero-sequence current is 2% of the base currents. And it agrees with the current frequency spectrum (left bar at 60 Hz, Fig. 8(a)).

Arm harmonic current can be calculated as  $(i_{au} - \frac{1}{3}i_a - \frac{1}{3}i_u)$ . As an example, the frequency spectrum of harmonic current in arm  $au$  is plotted in Fig. 10. As is expected, the arm harmonic current contains 20 Hz (circulating), 60 Hz (zero-sequence) and 100 Hz (circulating) components. There is also a small amount of 140 Hz component. It can be studied using the same method and including the higher order voltage ripples. When the capacitance is halved, similarly, harmonic magnitudes double. Again, the simulation result validates the theoretical analysis.

To compare the analytical formula with the simulation model, the calculated value (red) of the 40 Hz capacitor voltage ripple is plotted together with the measured ripple at 40 Hz in time domain simulation (black) in Fig 11. As can be seen, there is a good match between the two curves and therefore the calculated

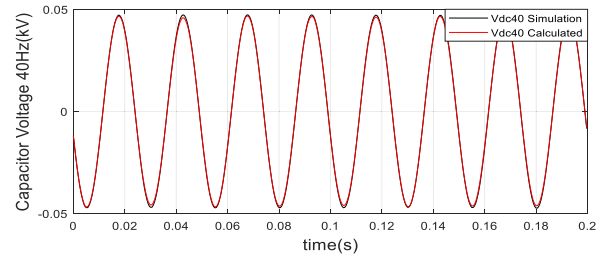


Fig. 11. Capacitor voltage 40 Hz – simulation result (black) and calculation value (red).

TABLE IV  
QUANTIZATION COMPARISON WITH SIMULATION RESULTS

Harmonic Component	Calculation Value (kA)	Simulation Value (kA)	Discrepancy (%)
60 Hz	0.014	0.012	16.7
100 Hz	0.007	0.009	22.2
20 Hz	0.004	0.005	20.0

value has high accuracy. In addition, the calculated values of harmonic currents are compared with the measured values in simulation and the results are shown in Table IV. It can be seen that the difference is only 0.001–0.002 kA. However, the values of harmonic currents are small so the discrepancy in percentage is around 20%. Hence, the current magnitude calculation is less accurate than the ripple voltage. Specifically, the calculated 60 Hz zero-sequence current is larger since theoretical analysis neglects resistance, with the presence of which, the actual current has a smaller value. For the 100 Hz and 20 Hz harmonic currents, the calculated values are smaller as expected, as theoretical analysis does not include the higher orders of the capacitor voltage ripple that can also lead to harmonic currents at 100 Hz and 20 Hz. For example, the 80 Hz voltage ripple interacts with the 20 Hz component in switching function and produces 100 Hz harmonics (80 + 20), or interacts with the 60 Hz component and produces 20 Hz harmonics (80–60).

## V. SUPPRESSION OF M<sup>3</sup>C HARMONICS

M<sup>3</sup>C harmonics can be controlled using hardware or software solutions. Based on the discussion in Section III, it is known that sub-module capacitance and arm inductance are affecting factors of the harmonics. So, proper values of the elements can be selected to limit the harmonics within a certain range. A detailed analysis is conducted in this section in order to provide instructions for capacitor and inductor values selection for the consideration of limiting harmonics. Also, delta connection could be an option for the grid-connecting transformer on the offshore side to deal with zero-sequence harmonic currents. The above measures are regarded as hardware methods to suppress M<sup>3</sup>C harmonics. On the other hand, an effective zero-sequence current mitigation control algorithm is proposed and tested for M<sup>3</sup>C in subsection B, which is indicated as a software method for harmonic suppression.

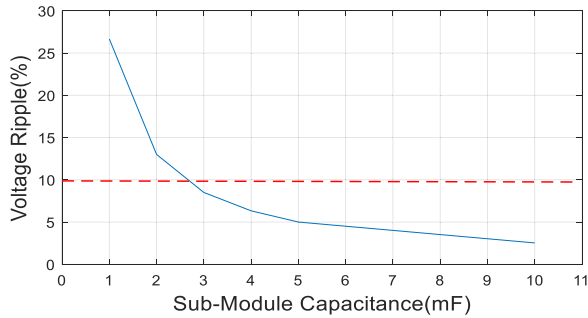


Fig. 12. Percentage voltage ripple versus sub-module capacitance.

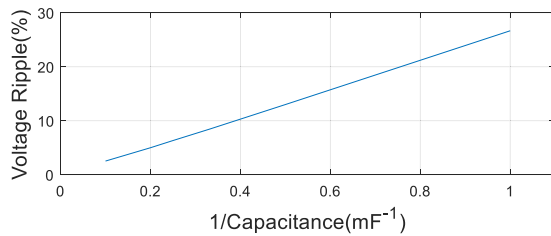
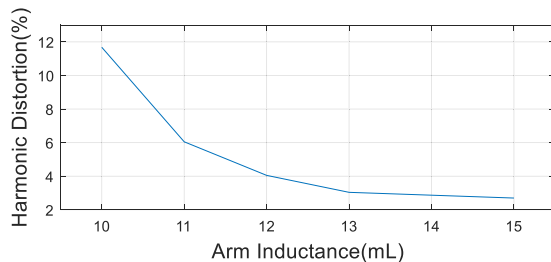

 Fig. 13. Percentage voltage ripple versus  $1/C$ .


Fig. 14. Grid side THD at different arm inductor values.

#### A. Proper Selection of Sub-Module Capacitance and Arm Inductance

At steady-state operation, it is normally considered that the voltage deviation should be kept within 10% of the DC sub-module capacitor voltage [35]. In Fig. 12, the capacitor voltage ripple is plotted against the sub-module capacitance for the test system. As can be seen, capacitance should be 3 mF or larger in this case to satisfy the maximum ripple requirement. In addition, the voltage ripple is plotted against the reciprocal of the capacitance. As is shown in Fig. 13, it is very closed to a perfect straight line, and therefore the time domain simulation confirms the quantified analysis.

Similarly, a suitable value should be selected for arm inductance to limit the total harmonic distortion (THD) within a certain level. The grid side THD is plotted with sub-module capacitance fixed at 5 mF and various arm inductances in Fig. 14. For instance, if THD needs to be limited lower than 10%, an arm inductance larger than 10.3 mL is required.

#### B. Zero-Sequence Current Mitigation Controller

In this sub-section, a zero-sequence current mitigation controller is proposed for  $M^3C$  and the control diagram is shown in Fig. 15. The principle is to use the  $M^3C$  to generate a

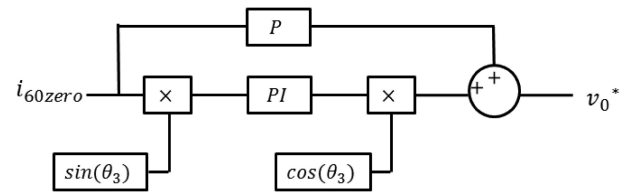
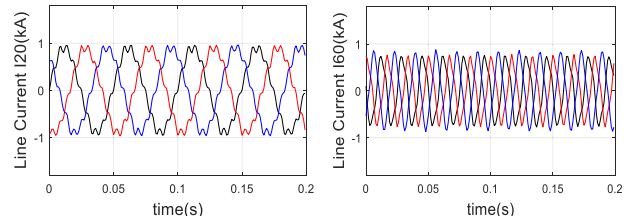
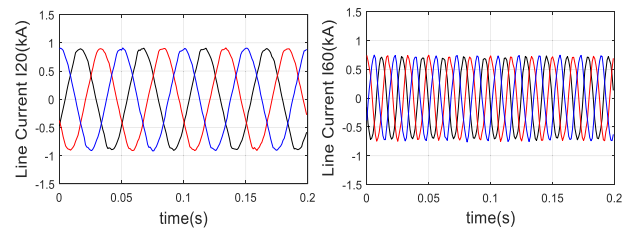


Fig. 15. Control diagram of the proposed zero-sequence current mitigation controller.



(a) Line currents before controller implemented



(b) Line currents after controller implemented

Fig. 16. Line currents at 20 Hz and 60 Hz sides before (a) and after (b) the zero-sequence current mitigation controller implementation.

compensating zero-sequence voltage  $v_0$  based on the measured zero-sequence current. The control purpose is to reduce the undesirable zero-sequence down to zero.  $\theta_3$  is the angle of the zero-sequence current and more details on the PLL for measuring it can be found in [36]. Considering that the zero-sequence harmonic currents are the same for all nine arms, only one controller is sufficient for all the arms in the  $M^3C$  to fulfill the control target.

In terms of controller parameters determination, gains cannot be too large for the mitigation controller. The reason is that the zero-sequence current mitigation control is an auxiliary control and it should not affect the primary vector control. If large gains are used, when the controller switches on, there would be a large zero-sequence voltage demand during the transient period. This zero-sequence voltage is superimposed to the voltage reference from vector control and may cause the converter to saturate. For illustrative purpose, a small sub-module capacitance is used (1 mF) to verify the effectiveness of the controller. Other parameters remain the same as in the last section. Controller parameters are available in the appendix. Note that besides 60 Hz, 180 Hz is also a prominent frequency that has zero-sequence current, so another controller is implemented based on the same principle. As can be seen in Fig. 16(a), the AC current waveforms at both sides are of poor quality. High order harmonics are salient at the 20 Hz side and the sinusoidal waveforms at the 60 Hz side are distorted. Fig. 16(b) shows the current waveforms after the mitigation control is implemented. A significant improvement can be seen. The zero-sequence current is plotted in Fig. 17 with the controller switched on at the beginning of the simulation.

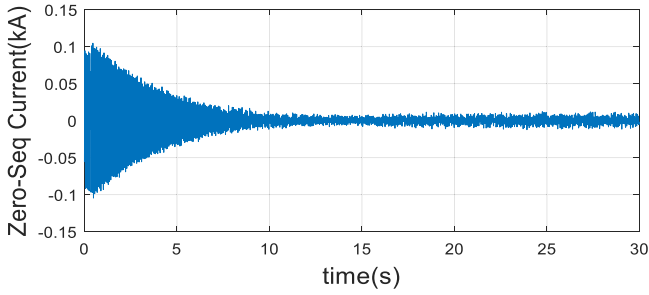


Fig. 17. Mitigation of zero-sequence current with controller switched on at the start of simulation.

It can be seen that with small gains, it may take seconds to fully suppress the zero-sequence current. But at steady state, the zero-sequence current can be mitigated to a negligible level and the effectiveness of the controller is verified.

## VI. CONCLUSION

As M<sup>3</sup>C is the core device in a FFTS, its harmonics have a considerable influence on the overall system performance. This paper has conducted a detailed harmonic analysis for M<sup>3</sup>C. Owing to the interaction between the switching function and the arm current at multiple frequencies, capacitor voltage ripples are induced on top of the DC voltage. It has been indicated that these ripples affect the arm voltages and further the arm currents. Also, it has been found that the arm currents contain harmonic components at 20 Hz, 60 Hz and 100 Hz and they have been analyzed respectively. The expressions of currents for all nine arms have been derived so that each component can be quantified. It has been found that several factors have large impact on the current harmonic magnitude, including capacitance, inductance and system operating frequency. The analysis has also revealed the nature of all the terms of the harmonic components. Some terms flow into AC systems at both sides, some terms are cancelled out and only exist in the arms, and the others have characteristics as fundamental currents and can be regulated by vector control. Zero-sequence components can cause instability problems, bringing risks of tripping zero-sequence protection, harmonics interaction and torsional oscillation. Both zero-sequence and circulating components take up current rating of the converter and have negative economic impact. They also bring extra losses, raise thermal issues and adversely affect the operation of other devices. Delta connection provides isolation on zero-sequence currents. In other cases, the harmonic currents can flow into the system or the generator and can cause a series of problems. The quantified calculation results have been compared with simulation results in RTDS and good matches have validated the theoretical analysis. Guidelines on sub-module capacitance and arm inductance have been provided to limit the capacitor voltage ripple and harmonic currents within a certain range. A zero-sequence current mitigation controller for M<sup>3</sup>C has been implemented and tested. Although the analysis has been carried out for FFTS in this paper, the procedure is general and can be beneficial to M<sup>3</sup>C modelling and control method development.

TABLE V  
MITIGATION CONTROLLER PARAMETERS

Symbol	Quantity	Value
$k_{p1}$	PI controller 1 proportional gain	1.0
$k_{i1}$	PI controller 1 integral gain	1.2
$k_{p2}$	P controller 2 proportional gain	0.2

## APPENDIX

### A. 20 Hz Arm Current Expressions

$$\begin{aligned}
 i_{au20\_2} &= k_4[m_a^2 I_a \sin(\theta_{10}) - m_a^2 I_u \sin(\theta_{11}) \\
 &\quad + m_a m_u I_a \sin(\theta_{12})] \\
 i_{av20\_2} &= k_4[m_a^2 I_a \sin(\theta_{10}) - m_a^2 I_u \sin(\theta_{11} - 120) \\
 &\quad + m_a m_u I_a \sin(\theta_{12} - 120)] \\
 i_{aw20\_2} &= k_4[m_a^2 I_a \sin(\theta_{10}) - m_a^2 I_u \sin(\theta_{11} + 120) \\
 &\quad + m_a m_u I_a \sin(\theta_{12} + 120)] \\
 &\quad \vdots \\
 i_{bu20\_2} &= k_4[m_a^2 I_a \sin(\theta_{10} - 120) - m_a^2 I_u \sin(\theta_{11}) \\
 &\quad + m_a m_u I_a \sin(\theta_{12})] \\
 &\quad \vdots \\
 i_{cw20\_2} &= k_4[m_a^2 I_a \sin(\theta_{10} + 120) - m_a^2 I_u \sin(\theta_{11} - 120) \\
 &\quad + m_a m_u I_a \sin(\theta_{12} - 120)]
 \end{aligned} \tag{A1}$$

where:  $k_4 = \frac{N}{24LC\omega^2}$ ;  $\theta_{10} = \omega_1 t + \beta_1$ ;  $\theta_{11} = \omega_1 t + \beta_3 - 2\alpha_1$ ;  
 $\theta_{12} = \omega_1 t + \alpha_3 - \beta_1 - \alpha_1$

$$\begin{aligned}
 i_{au20\_3} &= k_4[-m_u m_a I_a \sin(\theta_{13}) + m_u m_a I_u \sin(\theta_{14}) \\
 &\quad - m_u^2 I_a \sin(\theta_{15})] \\
 i_{av20\_3} &= k_4[-m_u m_a I_a \sin(\theta_{13} - 120) + m_u m_a I_u \sin(\theta_{14}) \\
 &\quad - m_u^2 I_a \sin(\theta_{15})] \\
 i_{aw20\_3} &= k_4[-m_u m_a I_a \sin(\theta_{13} + 120) + m_u m_a I_u \sin(\theta_{14}) \\
 &\quad - m_u^2 I_a \sin(\theta_{15})] \\
 &\quad \vdots \\
 i_{bu20\_3} &= k_4[-m_u m_a I_a \sin(\theta_{13}) + m_u m_a I_u \sin(\theta_{14} - 120) \\
 &\quad - m_u^2 I_a \sin(\theta_{15} - 120)] \\
 &\quad \vdots \\
 i_{cw20\_3} &= k_4[-m_u m_a I_a \sin(\theta_{13} - 120) + m_u m_a I_u \\
 &\quad \sin(\theta_{14} + 120) - m_u^2 I_a \sin(\theta_{15} + 120)]
 \end{aligned} \tag{A2}$$

where:  $\theta_{13} = \omega_1 t + \alpha_3 - \alpha_1 - \beta_1$ ;  $\theta_{14} = \omega_1 t + \alpha_3 - \beta_3 + \alpha_1$ ;  
 $\theta_{15} = \omega_1 t + \beta_1$

## REFERENCES

- [1] X. Xiang, M. Merlin, and T. Green, "Cost analysis and comparison of HVac, LFac and HVdc for offshore wind power connection," in *Proc. 12th IET Int. Conf. AC DC Power Transmiss.*, 2016, pp. 1–6.
- [2] X. Wang, "The fractional frequency transmission system," *Proc. IEEE 5th Annu. Conf. Jpn. Power Energy*, pp. 53–58, 1994.
- [3] J. Ruddy, R. Meere, and T. O'Donnell, "Low frequency ac transmission for offshore wind power: A review," *Renewable Sustain. Energy Rev.*, vol. 56, pp. 75–86, 2016.

- [4] CIGRE Working Group B4.55 Technical Brochure 619, "HVdc connection of offshore wind power plants," pp. 76–85, 2015.
- [5] S. Liu *et al.*, "Integrating offshore wind power via fractional frequency transmission system," *IEEE Trans. Power Del.*, vol. 32, no. 3, pp. 1253–1261, Jun. 2017.
- [6] X. Wang, X. Wei, and Y. Meng, "Experiment on grid-connection process of wind turbines in fractional frequency wind power system," *IEEE Trans. Energy Convers.*, vol. 30, no. 1, pp. 22–31, Mar. 2015.
- [7] J. Li and X.-P. Zhang, "Small signal stability of fractional frequency transmission system with offshore wind farms," *IEEE Trans. Sustain. Energy*, vol. 7, no. 4, pp. 1538–1546, Oct. 2016.
- [8] X. Wang, C. Cao, and Z. Zhou, "Experiment on fractional frequency transmission system," *IEEE Trans. Power Syst.*, vol. 21, no. 1, pp. 372–377, Feb. 2006.
- [9] S. Liu *et al.*, "A decoupled control strategy of modular multilevel matrix converter for fractional frequency transmission system," *IEEE Trans. Power Del.*, vol. 32, no. 4, pp. 2111–2121, Aug. 2017.
- [10] R. W. Erickson and O. A. Al-Naseem, "A new family of matrix converters," in *Proc. 27th Annu. Conf. IEEE Ind. Electron. Soc.*, vol. 2, 2001, pp. 1515–1520.
- [11] W. Kawamura, M. Hagiwara, and H. Akagi, "Control and experiment of a modular multilevel cascade converter based on triple-star bridge cells," *IEEE Trans. Ind. Appl.*, vol. 50, no. 5, pp. 3536–3548, Oct. 2014.
- [12] W. Kawamura *et al.*, "AC-inductors design for a modular multilevel TSBC converter, and performance of a low-speed high-torque motor drive using the converter," *IEEE Trans. Ind. Appl.*, vol. 53, no. 5, pp. 4718–4729, Oct. 2017.
- [13] M. Diaz *et al.*, "Modelling and control of the modular multilevel matrix converter and its application to wind energy conversion systems," in *Proc. 42nd Annu. Conf. IEEE Ind. Electron. Soc.*, 2016, pp. 5052–5057.
- [14] S. Liu, M. Saeedifard, and X. Wang, "Analysis and control of the modular multilevel matrix converter under unbalanced grid conditions," *IEEE J. Emerg. Sel. Topics Power Electron.*, vol. 6, no. 4, pp. 1979–1989, Dec. 2018.
- [15] Y. Miura *et al.*, "Modular multilevel matrix converter for low frequency ac transmission," in *Proc. IEEE 10th Int. Conf. Power Electron. Drive Syst.*, 2013, pp. 1079–1084.
- [16] F. Kammerer, J. Kolb, and M. Braun, "Fully decoupled current control and energy balancing of the modular multilevel matrix converter," in *Proc. 15th Int. Power Electron. Motion Control Conf.*, 2012, pp. LS2a. 3-1 - 3-8.
- [17] P. Sun *et al.*, "The harmonic analysis and the arm capacitor parameters selection of module multilevel matrix converter," in *Proc. IEEE PES Asia-Pacific Power Energy Eng. Conf.*, 2016, pp. 1617–1621.
- [18] J. Ma *et al.*, "Modular multilevel matrix converter for offshore low frequency ac transmission system," in *Proc. IEEE 26th Int. Symp. Ind. Electron.*, 2017, pp. 768–774.
- [19] L. Sainz *et al.*, "Effect of wind turbine converter control on wind power plant harmonic response and resonances," *IET Electric Power Appl.*, vol. 11, no. 2, pp. 157–168, 2017.
- [20] H. Saad *et al.*, "On resonances and harmonics in HVdc-MMC station connected to ac grid," *IEEE Trans. Power Del.*, vol. 32, no. 3, pp. 1565–1573, Jun. 2017.
- [21] C. Buchhagen *et al.*, "BorWin1 - First experiences with harmonic interactions in converter dominated grids," in *Proc. Int. ETG Congr.*, 2015, pp. 1–7.
- [22] T. Li, A. M. Gole, and C. Zhao, "Harmonic instability in MMC-HVdc converters resulting from internal dynamics," *IEEE Trans. Power Del.*, vol. 31, no. 4, pp. 1738–1747, Aug. 2016.
- [23] Q. Tu, Z. Xu, and L. Xu, "Reduced switching-frequency modulation and circulating current suppression for modular multilevel converters," *IEEE Trans. Power Del.*, vol. 26, no. 3, pp. 2009–2017, Jul. 2011.
- [24] E. Ebrahimzadeh *et al.*, "Harmonic instability source identification in large wind farms," in *Proc. IEEE Power Energy Soc. Gen. Meeting*, 2017, pp. 1–5.
- [25] N. P. Strachan and D. Jovicic, "Stability of a variable-speed permanent magnet wind generator with weak ac grids," *IEEE Trans. Power Del.*, vol. 25, no. 4, pp. 2779–2788, Oct. 2010.
- [26] X. Wang, F. Blaabjerg, and W. Wu, "Modeling and analysis of harmonic stability in an ac power-electronics-based power system," *IEEE Trans. Power Electron.*, vol. 29, no. 12, pp. 6421–6432, Dec. 2014.
- [27] W. Hu *et al.*, "Modeling and control of zero-sequence current in multiple grid connected converter," in *Proc. IEEE Power Electron. Spec. Conf.*, 2008, pp. 2064–2069.
- [28] B. Gao *et al.*, "Differential protection for an outgoing transformer of large-scale doubly fed induction generator-based wind farms," *Energies*, vol. 7, no. 9, pp. 5566–5585, 2014.
- [29] B. Zhang *et al.*, "Impact of wind farm integration on relay protection (6): Analysis of distance protection for wind farm outgoing transmission line," *Electric Power Automat. Equip.*, vol. 6, pp. 1–6, 2013.
- [30] M. Heathcote, *J & P Transformer Book*. New York, NY, USA: Elsevier, 2011.
- [31] M. Diaz *et al.*, "Control of wind energy conversion systems based on the modular multilevel matrix converter," *IEEE Trans. Ind. Electron.*, vol. 64, no. 11, pp. 8799–8810, Nov. 2017.
- [32] S. Eliban, Y. Zhang, and J. C. G. Alonso, "Real time simulation for HVdc grids with modular multi-level converters," in *Proc. 11th IET Int. Conf. AC DC Power Transmiss.*, 2015, pp. 1–8.
- [33] T. Maguire and J. Giesbrecht, "Small time-step VSC model for the real time digital simulator," in *Proc. Int. Conf. Power System Transients*, Montreal, QC, Canada, 2005, Paper IPST05-168.
- [34] S. Shang *et al.*, "Research on modeling and control strategy of modular multilevel matrix converter supplying passive networks," in *Proc. IEEE PES Asia-Pacific Power Energy Eng. Conf.*, 2016, pp. 1974–1978.
- [35] M. Zygmanski, B. Grzesik, and R. Nalepa, "Capacitance and inductance selection of the modular multilevel converter," in *Proc. 15th Eur. Conf. Power Electron. Appl.*, 2013, pp. 1–10.
- [36] Y. Wang *et al.*, "Open-winding power conversion systems fed by half-controlled converters," *IEEE Trans. Power Electron.*, vol. 28, no. 5, pp. 2427–2436, May 2013.



**Jiajie Luo** received the B.Eng. degrees from the Huazhong University of Science and Technology, Wuhan, China and the University of Birmingham, Birmingham, U.K., in 2015. He is currently working toward the Ph.D. degree with the University of Birmingham. He is currently working with Siemens Gamesa at its Power Converter Competence Center, U.K. His research interests include renewable energy integration, modeling, and control.



**Xiao-Ping Zhang** (M'95–SM'06) received the B.Eng., M.Sc., and Ph.D. degrees from Southeast University, in 1988, 1990 and 1993, respectively. He is currently a Professor of electrical power systems with the University of Birmingham, U.K. He is also the Director of Smart Grid, Birmingham Energy Institute and the Codirector of the Birmingham Energy Storage Center. He has coauthored the first and second edition of the monograph *Flexible AC Transmission Systems: Modeling and Control*, (Springer in 2006 and 2012). He has coauthored the book *Restructured Electric Power Systems: Analysis of Electricity Markets with Equilibrium Models*, (IEEE Press/Wiley in 2010). His research interests include modeling and control of HVdc/FACTS, renewable energy (wind/wave) control, distributed generation, energy storage and power economics, etc. Mr. Zhang is advisor to the IEEE PES U.K. and Ireland Chapter.



**Ying Xue** received the B.Eng. degree in electrical engineering from the Huazhong University of Science and Technology, Wuhan, China, and the University of Birmingham, Birmingham, U.K., in 2012, and the Ph.D. degree in electrical engineering from the University of Birmingham, in 2016. He is a Lecturer with the University of Birmingham. His main research area is HVdc modeling and control.



**Kanghui Gu** received the B.Eng. degree in electrical engineering from the Jiangsu University of Science and Technology, China, in 2014. He is currently working toward the Ph.D. degree in electrical engineering with Hohai University, Nanjing, China. He was a Visiting Student at the University of Birmingham between 2017 and 2018. His research interests include modeling and stability analysis of renewable energy generation.

**Feng Wu** photographs and biographies not available at the time of publication.